

# DIFFUSION GENERATIVE MODELS MEET COMPRESSED SENSING, WITH APPLICATIONS TO IMAGE DATA AND FINANCIAL TIME SERIES

ZHENGYI GUO, JIATU LI, WENPIN TANG, AND DAVID D. YAO

**ABSTRACT.** This paper develops dimension reduction techniques for accelerating diffusion model inference in the context of synthetic data generation. The idea is to integrate compressed sensing into diffusion models: (i) compress the data into a latent space, (ii) train a diffusion model in the latent space, and (iii) apply a compressed sensing algorithm to the samples generated in the latent space, facilitating the efficiency of both model training and inference. Under suitable sparsity assumptions on data, the proposed algorithm is proved to enjoy faster convergence by combining diffusion model inference with sparse recovery. As a byproduct, we obtain an optimal value for the latent space dimension. We also conduct numerical experiments on a range of datasets, including image data (handwritten digits, medical images, and climate data) and financial time series for stress testing.

*Key words:* Complexity, compressed sensing, diffusion models, inference time, signal recovery, sparsity.

## 1. INTRODUCTION

Diffusion models are a family of generative models that genuinely create the desired target distribution from noise [34, 68, 69]. They underpin the recent success in the text-to-image creators such as DALL·E 2 [60] and Stable Diffusion [61], and the text-to-video generators such as Sora [57], Make-A-Video [64] and Veo [29]. Despite their success in the domain of computer vision (and more recently, natural language processing [56, 40]), the use of diffusion models for data generation in other fields such as operations research and management remains underdeveloped. One main obstacle in applying diffusion models in traditional fields is that these models are often computationally demanding both in model training and generation/inference. For instance, generation may require hundreds to thousands of function evaluations (NFEs) in high-dimensional ambient spaces, with memory bandwidth and wall-clock time emerging as practical bottlenecks for with real-time and on-device deployment.

As observed in [25, 58], many existing data enjoy low-dimensional structures. So a natural solution to the aforementioned curse of dimensionality is to apply dimension reduction techniques to diffusion generative models. The pioneer work [38] proposed to efficiently train a diffusion model on a (suitable) *latent space* instead of directly on the ambient space, which triggers subsequent works on finding a (low-dimensional) latent space for diffusion model training (see e.g., [17, 19]). The focus of this paper is on accelerating diffusion generation with mild model training in the context of inference time scaling for diffusion models [53]. By exploiting the low-dimensional/sparse nature of the underlying dataset, we develop dimension reduction techniques for diffusion models, with applications to medical, climate and

---

*Date:* September 2, 2025.

financial data generation that may advance further analytical methods across domains such as supply chain logistics, healthcare, and energy systems.

The contributions of the paper are as follows:

- We develop a dimension reduction pipeline CSDM that combines diffusion models with compressed sensing [12, 13, 25]: (i) compress the data in  $\mathbb{R}^d$  into a low-dimensional (latent) space  $\mathbb{R}^m$  ( $d \gg m$ ); (ii) train a diffusion model in the compressed/latent space  $\mathbb{R}^m$  for inference; (iii) apply a compressed sensing algorithm to the samples generated in the latent space for decoding to  $\mathbb{R}^d$ .
- We provide theoretical analysis of CSDM by combining the diffusion inference time complexity with the compressed sensing recovery complexity. As a byproduct, we obtain an “optimal” value for the compressed (latent space) dimension, which offers a guidance on the choice of the space. For instance, in the very sparse setting, the commonly adopted DDPM model [34] with FISTA [3, 4] for recovery yields the complexity  $\mathcal{O}(\sqrt{d})$ , and the optimal compressed dimension  $m = \mathcal{O}(\sqrt{d})$ .
- We apply our proposed CSDM pipeline to various image dataset, including MNIST (handwritten digits), OCTMNIST (medical), and ERA5 Reanalysis (climate). In a separate direction, we combine diffusion models with principle component analysis (yet another dimension reduction technique) to generate financial time series for stress testing. In all these experiments, the proposed methodologies preserve high sample fidelity, while deliver substantial wall-clock speedups.

To the best of our knowledge, this is the first paper to combine diffusion models with compressed sensing for accelerating the inference process. The intuition is clear: score evaluation, backpropagation, and sampling scale with the compressed dimension  $m \ll d$ , which facilitate the efficiency of both training and inference. In terms of applications, our pipeline is designed for decision-centric workflows that require large scenario sets under tight compute budgets. As an example, in climate and energy systems, we often generate compressed-domain ensembles of gridded weather fields (e.g., precipitation and irradiance), and decode only the subsets needed for unit commitment, reserve sizing, and chance-constrained optimal power flow, thereby enabling denser Monte-Carlo and what-if studies within the same wall-clock budget. We also note that the CSDM pipeline can be easily integrated into diffusion model fine-tuning/post-training/alignment [6, 26, 83] (see [79, Section 4.5] for a review), which will be the focus of our future work. Notably, the recent work [39] shows promise in using a coarser model such as CSDM (a “bad” version) for fine-tuning diffusion models.

**Related Literature:** Here we provide a brief review of the most relevant works. Diffusion models were proposed by [34, 68, 69] in the context of generative modeling, which have been shown to empirically outperform other generative models such as GANs on various synthetic tasks [24, 42]. Subsequent works studied the convergence of diffusion models [21, 27, 47], just to name a few (see Section 2.1 for more references). As mentioned earlier, training diffusion models often suffers from the curse of dimensionality. This leads to the works of finding provably good latent spaces for diffusion model training [17, 19]. There are also numerous works on accelerating diffusion model inference, including deterministic sampling [65], higher-order ODE solvers [52, 82], and progressive/consistency distillation [63, 66, 67]. These sampling methods can be applied to diffusion inference in the latent space, hence being easily integrated into our CSDM framework. Recently, a line of theoretical works [36, 48, 59]

explored the diffusion’s capability of adapting to low dimensionality. That is, a diffusion model itself can capture the data’s low-dimensional structure and yields faster convergence, even without any dimension reduction tricks. The main difference is that these works still require model training in the ambient space, while we propose to train the model in the latent space for more efficient training. Refer to Section 3 for further discussions. Finally, the literature of compressed sensing [12, 13, 25] is reviewed in Section 2.2. We also point out that in another direction [8, 80], generative models are used for efficiently solving the inverse problems (e.g., compressed sensing). This is different from our setting, where compressed sensing *helps* accelerate data generation.

**Organization of the paper:** The remainder of the paper is organized as follows. Section 2 gives background on diffusion models and compressed sensing. Our CSDM methodology and its theory are developed in Section 3. In Sections 4–5, we provide numerical experiments on image and financial time series data. Concluding remarks are summarized in Section 6.

## 2. PRELIMINARIES

This section provides background on the two key objects of the paper, diffusion models and compressed sensing.

Below we collect some notations that will be used throughout this paper.

- For  $x, y \in \mathbb{R}^d$ ,  $x \cdot y$  denote the inner product between  $x$  and  $y$ , and  $|x|_p := (\sum_{i=1}^d |x^i|^p)^{1/p}$  is the  $p$ -norm of  $x$ .
- For a function  $f : \mathbb{R}^d \rightarrow \mathbb{R}$ , let  $\nabla f$  denote the gradient of  $f$ .
- The symbol  $\mathcal{N}(\mu, \Sigma)$  denotes the Gaussian distribution with mean  $\mu$  and covariance matrix  $\Sigma$ , and  $\text{Unif}[a, b]$  denotes the uniform distribution on  $[a, b]$ .
- For  $f : \mathbb{R}^d \rightarrow \mathbb{R}^m$  and  $\mu(\cdot)$  a probability measure on  $\mathbb{R}^d$ , the symbol  $f_{\#}\mu(\cdot)$  denotes the pushforward of  $\mu(\cdot)$  by  $f$ .
- The symbol  $a = \mathcal{O}(b)$  or  $a \lesssim b$  means that  $a/b$  is bounded as some problem parameter tends to 0 or  $\infty$  (often neglecting the logarithmic factor).

**2.1. Diffusion models.** Diffusion models are a class of generative models that learn data distributions by a two-stage procedure: the *forward process* gradually adding noise to data, and the *reversed process* recovering/generating the data distribution  $p_{\text{data}}(\cdot)$  from noise. There are many formulations of diffusion models, e.g., by Markov chains [34, 68], by stochastic differential equations (SDEs) [69], and by deterministic flows [50, 51]. To provide context, we briefly review the continuous-time formulation by SDEs that offers a unified framework of diffusion models.

We follow the presentation of [73]. The forward process is governed by an SDE:

$$dX_t = f(t, X_t)dt + g(t)dW_t, \quad X_0 \sim p_{\text{data}}(\cdot), \quad (2.1)$$

where  $f : \mathbb{R}_+ \times \mathbb{R}^d \rightarrow \mathbb{R}^d$ ,  $g : \mathbb{R}_+ \rightarrow \mathbb{R}_+$ , and  $(W_t)_{t \geq 0}$  is Brownian motion in  $\mathbb{R}^d$ . Some conditions are required on  $f(\cdot, \cdot)$  and  $g(\cdot)$  so that the SDE (2.1) is well-defined, and that  $X_t$  has a smooth density  $p(t, x) := \mathbb{P}(X_t \in dx)/dx$ , see [70]. As a notable example,  $f(t, x) = -\frac{1}{2}(at+b)x$  and  $g(t) = \sqrt{at+b}$  for some  $a, b > 0$  corresponds to the *variance preserving* (VP) model [69], whose discretization yields the most widely used *denoising diffusion probabilistic models* (DDPMs) [34].

The key to the success of continuous diffusion models is that their time reversal  $(\tilde{X}_t)_{0 \leq t \leq T}$  has a tractable form:

$$d\tilde{X}_t = \left( -f(T-t, \tilde{X}_t) + g^2(T-t) \nabla \log p(T-t, \tilde{X}_t) \right) dt + g(T-t) dB_t, \quad \tilde{X}_0 \sim p(T, \cdot),$$

with  $(B_t)_{t \geq 0}$  a copy of Brownian motion in  $\mathbb{R}^d$  [33]. It is common to replace  $p(T, \cdot)$  with a noise  $p_{\text{noise}}(\cdot)$ , which is close to  $p(T, \cdot)$  but should *not* depend on  $p_{\text{data}}(\cdot)$ . All but the term  $\nabla \log p(T-t, \tilde{X}_t)$  are available, so it comes down to learning  $\nabla \log p(t, x)$ , known as *Stein's score function*. Recently developed score-based methods attempt to approximate  $\nabla \log p(t, x)$  by neural nets  $\{s_\theta(t, x)\}_\theta$ , called *score matching*. The resulting reversed process  $(Y_t)_{0 \leq t \leq T}$  is:

$$dY_t = \left( -f(T-t, Y_t) + g^2(T-t) s_\theta(T-t, Y_t) \right) dt + g(T-t) dB_t, \quad Y_0 \sim p_{\text{noise}}(\cdot). \quad (2.2)$$

An equivalent probabilistic ODE sampler is:

$$dY_t = \left( -f(T-t, Y_t) + \frac{1}{2} g^2(T-t) s_\theta(T-t, Y_t) \right) dt, \quad Y_0 \sim p_{\text{noise}}(\cdot). \quad (2.3)$$

Both (2.2) and (2.3) are referred to as the *inference processes*, and the implementation requires discretizing these processes.

There are several existing score matching methods, among which the most widely used one is *denoising score matching* (DSM) [77]:

$$\min_{\theta} \mathbb{E}_{t \sim \text{Unif}[0, T]} \left\{ \lambda_t \mathbb{E}_{X_0 \sim p_{\text{data}}} \left[ \mathbb{E}_{p(t, \cdot | X_0)} \left| s_\theta(t, X_t) - \nabla \log p(t, X_t | X_0) \right|_2^2 \right] \right\}, \quad (2.4)$$

where  $\lambda_t$  is a weight function. The advantage of DSM is that most existing models (e.g., VP) are Gaussian processes of form  $X_t = \alpha_t X_0 + \sigma_t \varepsilon$ , with  $\varepsilon \sim \mathcal{N}(0, I)$  independent of  $X_0$ . By adopting a noise parameterization  $\varepsilon_\theta(t, X_t) = -\sigma_t s_\theta(t, X_t)$ , DSM (2.4) reduces to:

$$\min_{\theta} \mathbb{E}_{t \sim \text{Unif}[0, T]} \left[ \frac{\lambda_t}{\sigma_t^2} \mathbb{E}_{X_0 \sim p_{\text{data}}, \varepsilon \sim \mathcal{N}(0, I)} \left| \varepsilon_\theta(t, \alpha_t X_0 + \sigma_t \varepsilon) - \varepsilon \right|_2^2 \right]. \quad (2.5)$$

Common choices for the weight function are  $\lambda_t = \sigma_t^2$  [69], and  $\lambda_t = -\sigma_t^2 \left( \log \frac{\alpha_t^2}{\sigma_t^2} \right)'$  [41] corresponding to the evidence lower bound. For theoretical studies, it is standard to assume a blackbox score matching error: there is  $\epsilon > 0$  such that

$$\mathbb{E}_{X \sim p(t, \cdot)} \left| s_{\theta_*}(t, X) - \nabla \log p(t, X) \right|_2^2 < \epsilon^2, \quad (2.6)$$

where  $\theta_*$  is output by some score matching algorithm (e.g., DSM (2.4) or (2.5)). See also [18, 31, 78] for analysis of score matching errors based on specific neural network structures.

It is expected that under suitably good score matching, the output  $Y_T$  or its discretization of the models (2.2) and (2.3) is close to  $p_{\text{data}}(\cdot)$ . To simplify the presentation, we focus on the VP model and its discretization. We need the following result on the  $W_2$  convergence of the model.

**Theorem 2.1.** *Let  $(Y, \tilde{Y})$  be defined on the same probability space such that  $Y \sim p_{\text{data}}(\cdot)$ , and  $Y'$  is distributed as the output of the VP model. Assume that  $p_{\text{data}}(\cdot)$  is strongly log-concave, the score  $\nabla \log p(t, x)$  is Lipschitz, and the score matching error (2.6) holds. Then:*

- (1) [27] *There is a discretization of (2.2) such that it takes  $n_{\text{diff}} = \mathcal{O}(\frac{d}{\epsilon^2})$  steps to achieve  $|Y - \tilde{Y}|_2 \leq \epsilon$  with high probability.*

(2) [28] *There is a discretization of (2.3) such that it takes  $n_{\text{diff}} = \mathcal{O}(\frac{\sqrt{d}}{\epsilon})$  steps to achieve  $|Y - \tilde{Y}|_2 \leq \epsilon$  with high probability.*

The  $W_2$  convergence of other diffusion models, e.g., variance exploding (VE) [69], was also studied in [27, 28, 72]. See also [5, 20, 21, 45, 46, 47, 49] for the KL convergence under similar assumptions as in Proposition 2.1. In another direction, [36, 48, 59] explored the adaptivity of diffusion models to (unknown) low dimensionality. They showed that it takes  $\mathcal{O}(\frac{d_{\text{IS}}}{\epsilon^2})$  steps, where  $d_{\text{IS}}$  is the *intrinsic dimension*, for DDPM to achieve an  $\epsilon$  KL-error. We defer the discussion to Section 3.

**2.2. Compressed sensing.** Compressed sensing [10, 12, 13, 25] offers a powerful framework for the exact recovery of a *sparse* signal  $x \in \mathbb{R}^d$  from a limited number of observations  $y \in \mathbb{R}^m$  with  $m \ll d$ . We start by reviewing compressed sensing, following the presentation of [9].

*Sparse recovery problem:* Let  $x = (x^1, \dots, x^d)$ , and assume that its support  $T := \{i : x^i \neq 0\}$  has small cardinality. The primary goal is to solve:

$$\min |x|_0 \quad \text{subject to} \quad Ax = y. \quad (2.7)$$

Solving this problem is equivalent to finding sparse solutions to an underdetermined system of linear equations, which is NP-hard [55]. The key idea of compressed sensing relies on  $L^1$  techniques; that is to transform the problem (2.7) into a linear program:

$$\min |x|_1 \quad \text{subject to} \quad Ax = y, \quad (2.8)$$

which is known as *basis pursuit* [22].

In our application, we do not have exact compressed data  $y$ . Instead, we have synthetic generation  $\tilde{y}$  that can be viewed as a measurement with noise. This scenario fits into *robust compressed sensing* [11]:  $y = Ax + e$ , where  $e$  is some unknown perturbation with  $|e|_2 \leq \sigma$  ( $\sigma$  is known). It is natural to consider the convex program:

$$\min |x|_1 \quad \text{subject to} \quad |Ax - y|_2 \leq \sigma. \quad (2.9)$$

In fact, the solution to (2.9) recovers a sparse signal with an error at most of the noise level. To state the result, we need the following notion.

**Definition 2.2.** [12] *Let  $A$  be the matrix with the finite collection of vectors  $(v_j)_{j \in J} \in \mathbb{R}^m$  as columns. For each  $1 \leq S \leq |J|$ , we define the  $S$ -restricted isometry constant  $\delta_S$  to be the smallest quantity such that  $A_T$  obeys*

$$(1 - \delta_S)|c|_2^2 \leq |A_T c|_2^2 \leq (1 + \delta_S)|c|_2^2,$$

for all subsets  $T \subset J$  of cardinality at most  $S$ , and all real coefficients  $(c_j)_{j \in T}$ .

The numbers  $\delta_S$  measure how close the vectors  $v_j$  behave like an orthonormal system, but only when restricting to sparse linear combinations involving no more than  $S$  vectors. The following theorem concerns sparse recovery for robust compressed sensing.

**Theorem 2.3.** [11] *Let  $S$  be such that  $\delta_{3S} + 3\delta_{4S} < 2$ . Then for any signal  $x$  supported on  $T$  with  $|T| \leq S$  (referred to as  $S$ -sparse), and any perturbation  $e$  with  $|e|_2 \leq \sigma$ ,*

$$|x_* - x|_2 \leq C_S \sigma,$$

where  $x_*$  is the solution to the problem (2.9), and the constant  $C_S$  only depends on  $\delta_{4S}$ .

*Sparse recovery optimization:* The task is to solve numerically the optimization problem (2.9). It is known that this problem can be recast into an unconstrained convex problem:

$$\min \frac{1}{2} \|Ax - y\|_2^2 + \lambda \|x\|_1, \quad (2.10)$$

where the relation between  $\lambda$  and  $\sigma$  is specified by the Pareto frontier [75]. The problem (2.10), known as Lasso or image deblurring problem, can be solved by several iterative algorithms. Here we focus on one of these algorithms, *Fast Iterative Shrinkage-Thresholding Algorithm* (FISTA) [3, 4].

In the sequel, we denote  $f(x) := \frac{1}{2} \|Ax - y\|_2^2$  and  $g(x) := \lambda \|x\|_1$ . Note that  $\nabla f(x) = A^T(Ax - y)$ , so

$$\|\nabla f(x) - \nabla f(x')\|_2 \leq L \|x - x'\|_2 \quad \text{for all } x, x' \in \mathbb{R}^d, \quad (2.11)$$

where  $L := \lambda_{\max}(A^T A)$  is the largest eigenvalue of  $A^T A$ . Define

$$Q_L(x, x') := f(x') + \nabla f(x') \cdot (x - x') + \frac{L}{2} \|x - x'\|_2^2 + g(x),$$

and

$$\begin{aligned} p_L(x') &= \arg \max_x Q_L(x, x') \\ &= \arg \max_x \left\{ \frac{L}{2} \left\| x - \left( x' - \frac{\nabla f(x')}{L} \right) \right\|_2^2 + g(x) \right\} \\ &= \text{SoftThreshold} \left( x' - \frac{\nabla f(x')}{L}, \frac{\lambda}{L} \right), \end{aligned} \quad (2.12)$$

where the soft-thresholding operator is applied coordinate-wise [15, 23]:

$$\text{SoftThreshold}(x, a)_i := \begin{cases} x_i - a & \text{if } x_i > a, \\ 0 & \text{if } |x_i| \leq a, \\ x_i + a & \text{if } x_i < -a. \end{cases}$$

FISTA is a proximal gradient method by incorporating the Nesterov acceleration.

#### Fast Iterative Shrinkage-Thresholding Algorithm (FISTA)

**Input:**  $L$  (Lipschitz constant of  $\nabla f$ ).

**Step 0.** Take  $y_1 = x_0 \in \mathbb{R}^d$ ,  $t_1 = 1$ .

**Step k.** Compute

$$\begin{aligned} x_k &= p_L(y_k), \\ t_{k+1} &= \frac{1 + \sqrt{1 + 4t_k^2}}{2}, \\ y_{k+1} &= x_k + \left( \frac{t_k - 1}{t_{k+1}} \right) (x_k - x_{k-1}). \end{aligned}$$

FISTA is a proximal gradient method by incorporating Nesterov acceleration. The convergence result is as follows.

**Theorem 2.4.** [3, 7] *Let  $x_*$  be the solution to the problem (2.10), and  $\{x_k\}_{k \geq 0}$  the FISTA iterates. We have for  $k$  sufficiently large,*

$$F(x_k) - F(x^*) \leq \frac{CL}{k^2} \quad \text{and} \quad |x_k - x_*|_2 \leq \frac{C(L + |y|_2)}{k},$$

for some  $C > 0$ .

To ensure that  $|x_k - x_*|_2 \leq \epsilon$ , it requires the number of iterations  $n_{\text{CS}} = \mathcal{O}\left(\frac{L}{\epsilon}\right) = \mathcal{O}\left(\frac{s_{\max}^2(A)}{\epsilon}\right)$ , where  $s_{\max}(A)$  is the largest singular value of  $A$ . Also refer to [37, 74] for sharper convergence results of FISTA (but implicit in the dependence on dimension).

### 3. MAIN RESULTS

In this section, we develop the methodology by combining diffusion models with compressed sensing for sparse signal/data generation, and provide theoretical insights. As mentioned in the introduction, the idea is to compress the data into a lower dimension space, where a diffusion model is employed to generate samples more efficiently. Compressed sensing is then used to convert the generated samples in the latent space to the original signal/data space. Our algorithm is summarized as follows.

#### Compressed Sensing + Diffusion models (CSDM)

**Input:**  $A \in \mathbb{R}^{m \times d}$  (sketch matrix,  $m \ll d$ ).

**Step 1.** Apply linear sketch to compress the data  $p_{\text{data}}(\cdot)$  in  $\mathbb{R}^d$  into  $\tilde{p}_{\text{data}}(\cdot) := A_{\#} p_{\text{data}}(\cdot)$  in  $\mathbb{R}^m$ .

**Step 2.** Train a diffusion model using the data points drawn from  $\tilde{p}_{\text{data}}(\cdot)$ .

**Step 3.** Apply FISTA to solve the problem (2.10), with  $y$  generated by the diffusion model trained in Step 2.

Though Algorithm CSDM can be applied to any target data, it is mostly efficient for generating sparse data distribution in the regime of compressed sensing. The following theorem provides a theoretical guarantee for the use of CSDM in data generation.

**Theorem 3.1.** *Let  $(x, \tilde{y})$  be defined on the same probability space such that  $x \sim p_{\text{data}}(\cdot)$ , and  $\tilde{y}$  is output by the diffusion model in Algorithm CSDM. Assume that  $|Ax - \tilde{y}|_2 \leq \sigma$  with high probability. Also let the assumptions in Theorem 2.3 hold (i.e.,  $p_{\text{data}}(\cdot)$  enjoys  $S$ -sparsity). For  $\{x_k\}_{k \geq 0}$  the FISTA iterates as to  $\tilde{y}$ , we have with high probability,*

$$|x_k - x|_2 \leq C \left( \sigma + \frac{s_{\max}^2(A) + \sqrt{S}}{k} \right), \quad \text{for } k \text{ sufficiently large,} \quad (3.1)$$

where  $s_{\max}(A)$  is the largest singular value of  $A$ .

*Proof.* Let  $x_*$  be the solution to the problem:

$$\min |x|_1 \quad \text{subject to} \quad |Ax - \tilde{y}|_2 \leq \sigma.$$

By Theorem 2.3, we have  $|x - x_*|_2 \leq C\sigma$  for some  $C > 0$ . Further by Theorem 2.4, we have for  $k$  sufficiently large,

$$|x_k - x_*|_2 \leq \frac{C(L + |\tilde{y}|_2)}{k} \leq \frac{C(L + \sigma + |Ax|_2)}{k}.$$

Under the assumption of Theorem 2.3, the term  $|Ax|_2$  is of order  $\mathcal{O}(\sqrt{S})$ . Thus, we get  $|x_k - x_*|_2 \leq \frac{C(L+\sigma+\sqrt{S})}{k}$  for  $k$  sufficiently large. By triangle inequality, we have  $|x_k - x|_2 \leq |x_k - x_*|_2 + |x_* - x|_2$ , which yields the desired result.  $\square$

Specializing to the VP model leads to the following corollary.

**Corollary 3.2.** *Let the assumptions in Theorem 2.1 and Theorem 3.1 hold, with  $\tilde{y}$  be the output of the discretized VP model in  $k'$  steps, and  $\{x_{k',k}\}_{k \geq 0}$  be the FISTA iterates as to  $\tilde{y}$ . Then:*

(1) *Using the stochastic sampler (2.2), we have for  $k, k'$  sufficiently large,*

$$|x_{k,k'} - x|_2 \leq C \left( \sqrt{\frac{m}{k'}} + \frac{s_{\max}^2(A) + \sqrt{S}}{k} \right), \quad \text{for some } C > 0. \quad (3.2)$$

(2) *Using the deterministic sampler (2.3), we have for  $k, k'$  sufficiently large,*

$$|x_{k,k'} - x|_2 \leq C \left( \frac{\sqrt{m}}{k'} + \frac{s_{\max}^2(A) + \sqrt{S}}{k} \right), \quad \text{for some } C > 0. \quad (3.3)$$

Several remarks are in order:

(a) It is common to choose the sketch matrix  $A \in \mathbb{R}^{m \times d}$  to be random, e.g., each entry of  $A$  is a Gaussian variable with mean 0 and variance  $\frac{1}{m}$ . By extreme value theory of random matrices [62], the largest singular value

$$s_{\max}(A) \lesssim \sqrt{\frac{d}{m}} \quad \text{with high probability.}$$

Thus, the Lipschitz constant  $L = s_{\max}^2(A)$  is of order  $\frac{d}{m}$ . Replacing  $s_{\max}^2(A)$  with  $\frac{d}{m}$  in (3.2)-(3.3) yields:

$$|x_{k,k'} - x|_2 \lesssim \begin{cases} \sqrt{\frac{m}{k'}} + \frac{1}{k} \left( \frac{d}{m} + \sqrt{S} \right) & \text{for the stochastic sampler,} \\ \frac{\sqrt{m}}{k'} + \frac{1}{k} \left( \frac{d}{m} + \sqrt{S} \right) & \text{for the deterministic sampler.} \end{cases} \quad (3.4)$$

(b) The two terms in the bounds (3.2), (3.3) and (3.4) correspond to the *diffusion sampling error* and the *compressed sensing optimization error*. As mentioned in the introduction, a tradeoff between these two errors leads to an optimal choice of  $m$  – the compressed data dimension. Let's take the stochastic sampler of the VP model for example. In order to get  $|x_{k,k'} - x|_2 \leq \epsilon$ , it requires:

$$k' = \mathcal{O}\left(\frac{m}{\epsilon^2}\right) \quad \text{and} \quad k = \mathcal{O}\left(\left(\frac{d}{m} + \sqrt{S}\right) \frac{1}{\epsilon}\right)$$

Also assume that in each iteration, the computational cost of diffusion sampling is comparable to that of compressed sensing optimization. Under this hypothesis, the complexity that combines sampling and optimization is of order:

$$\max\left(m, \frac{d}{m} + \sqrt{S}\right). \quad (3.5)$$

Consider the very sparse case  $S = \mathcal{O}(1)$ . Optimizing (3.5) with respect to  $m$  yields  $m = \mathcal{O}(\sqrt{d})$ , with the resulting complexity  $\mathcal{O}(\sqrt{d})$ . Similarly, for the deterministic sampler of the VP model, the optimal  $m = \mathcal{O}(d^{\frac{2}{3}})$ , with the resulting complexity  $\mathcal{O}(d^{\frac{1}{3}})$ .

(c) Theorem 3.1 is flexible to support different sampling schemes and optimization algorithms. Also assume that  $S = \mathcal{O}(1)$ . Table 1 below summarizes the optimal  $m$  and corresponding complexity under various sampling methods with FISTA for compressed sensing.

Sampling	VP (Det.)	VP (Stoc.)	VE (Det.)	VE (Stoc.)
$m$	$d^{\frac{2}{3}}$	$d^{\frac{1}{2}}$	$d^{\frac{2}{5}}$	$d^{\frac{2}{3}}$
Complexity	$d^{\frac{1}{3}}$	$d^{\frac{1}{2}}$	$d^{\frac{3}{5}}$	$d^{\frac{1}{3}}$

TABLE 1. Optimal  $m$  and the corresponding complexity under different sampling schemes and FISTA for compressed sensing. Det. (resp. Stoc.) is short for deterministic (resp. “stochastic”).

There are also other (provable) optimization algorithms for solving compressed sensing (2.10). For instance, *iteratively reweighted least squares* (IRLS) [14, 16, 30] was proved to achieve the computational complexity  $\mathcal{O}\left(\frac{d}{\sqrt{m}}\right)$  [43]. So for the VP model, the stochastic sampler with IRLS for compressed sensing yields the optimal  $m = d^{\frac{2}{3}}$  and the complexity  $\mathcal{O}(d^{\frac{1}{3}})$ ; and the deterministic sampler with IRLS for compressed sensing yields the optimal  $m = \mathcal{O}(d)$  and the complexity  $\mathcal{O}(d^{\frac{1}{2}})$ .

(d) As mentioned earlier, a recent line of works [36, 48, 59] studied the diffusion model’s capability of adapting to low dimensionality. It was shown that the complexity (in KL) of DDPM, a version of the stochastic sampler of the VP model, is  $\mathcal{O}(d_{\text{IS}})$ , where  $d_{\text{IS}}$  is the intrinsic dimension defined as the logarithm of the data’s metric entropy. Under the  $S$ -sparsity assumption, it is known [76] that

$$d_{\text{IS}} = \mathcal{O}(S \log d). \quad (3.6)$$

This yields the complexity  $\mathcal{O}(S \log d)$  for DDPM in KL divergence.

On the other hand, it requires  $m \gtrsim S$  to ensure that  $A$  satisfies the  $S$ -restricted isometry property. It then follows from (3.5):

$$\text{the complexity of CSDM} = \begin{cases} \mathcal{O}(S) & \text{if } S \gtrsim \sqrt{d}, \\ \mathcal{O}(\sqrt{d}) & \text{if } S \lesssim \sqrt{d}. \end{cases} \quad (3.7)$$

If the results of [36, 48, 59] also hold in  $L^2$  norm, then our proposed CSDM achieves the same complexity as theirs when  $S \gtrsim \sqrt{d}$ . Note that sharper bounds on the FISTA convergence (e.g., independent of  $S$ ) will lead to a better complexity for CSDM than that of a diffusion model alone. Moreover, diffusion models are typically easier to train in low-dimensional spaces than in high-dimensional settings. We also mention the work [17], which proposed to project data onto a low-dimensional space for efficient score matching, as opposed to direct generation.

#### 4. NUMERICAL EXPERIMENTS ON IMAGE DATA

In this section, we conduct numerical experiments on various sparse image datasets, including handwritten digits (MNIST), medical images (OCTMNIST), and climate images (ERA5 Reanalysis). Generating such data plays an important role in advancing further analytical methodologies across domains such as supply chain logistics, healthcare, and energy systems.

Due to the inherently low resolution of publicly available datasets (e.g., MNIST and OCTMNIST), we adopt a *resolution upscaling strategy*: all images are resized to larger spatial dimensions, while preserving their inherent sparsity structure. This ensures that the dimensionality is sufficiently high to corroborate our proposed CSDM framework. Upscaling is applied only to form the ambient dimension  $d$  for time comparisons, whereas the compressed dimension  $m$  is fixed across all  $d$ . Take the MNIST dataset for instance: we fix the sketch matrix  $A \in \mathbb{R}^{m \times d}$  across all experiments for each  $d \in \{32 \times 32, 40 \times 40, 48 \times 48\}$ , where  $m = 28^2 = 784$  is the compressed dimension. This allows us to evaluate our method under varying degrees of compression, corresponding to 77%, 49%, and 34% respectively.

In our proposed pipeline, the total generation time per image consists of:

- (1) *Diffusion inference time*  $T_{\text{diff}}^{(m)}$ : the inference time of the diffusion model in  $\mathbb{R}^m$ .
- (2) *Recovery time*  $T_{\text{CS}}^{(m,d)}$ : the time required for compressed sensing ( $\mathbb{R}^m \rightarrow \mathbb{R}^d$ ) via FISTA.

So the total generation time of our algorithm is  $T_{\text{total}} = T_{\text{diff}}^{(m)} + T_{\text{CS}}^{(m,d)}$ . Our goal is to measure the speedup over the baseline, which is to perform diffusion inference directly in  $\mathbb{R}^d$ . Here we adopt the stochastic sampler, so  $T_{\text{diff}}^{(d)} \approx \frac{d}{m} \cdot T_{\text{diff}}^{(m)}$  (see Theorem 2.1). Then, the speedup is computed as:

$$\text{Speedup} = 1 - \frac{T_{\text{total}}}{T_{\text{diff}}^{(d)}} = 1 - \left( \frac{m}{d} + \frac{m}{d} \frac{T_{\text{CS}}^{(m,d)}}{T_{\text{diff}}^{(m)}} \right). \quad (4.1)$$

**4.1. Results on MNIST.** The MNIST dataset [44] consists of images of handwritten digits, and on average, over 80% of the pixels in each image have intensity values equal or very close to zero. As mentioned, we resize the images to the ambient resolutions  $d \in \{32 \times 32, 40 \times 40, 48 \times 48\}$ , and fix the compressed dimension at  $m = 28 \times 28$ . We train a VP model in  $\mathbb{R}^m$  for diffusion inference, and decode the generated sample to  $\mathbb{R}^d$  by FISTA.

Table 2 reports per-image wall-clock for (i) diffusion inference in  $\mathbb{R}^m$  and (ii) FISTA recovery in  $\mathbb{R}^d$ , along with the speedup. As the ambient dimension  $d$  increases (or the retention  $m/d$  drops), the diffusion inference time in the latent space  $\mathbb{R}^m$  stays roughly constant with the recovery adding a small overhead, while the diffusion inference in the ambient space grows with  $d$ . This leads to increasing net speedups (from 4.39% up to 61.13%).

Compression	Original Dim.	Original Dim. Inference Time	Low Dim. Inference Time	Recovery Time	Speedup
76%	1024 $\rightarrow$ 784	0.4463s / pic	0.3417s / pic	0.0852s / pic	<b>4.39%</b>
49%	1600 $\rightarrow$ 784	1.1103s / pic	0.5441s / pic	0.0741s / pic	<b>44.32%</b>
34%	2304 $\rightarrow$ 784	1.5987s / pic	0.5440s / pic	0.0774s / pic	<b>61.13%</b>

TABLE 2. Comparison of generation time on MNIST

Figure 1 illustrates CSDM generations at each compression level. With low compression/high retention (76%), digits are crisp and legible with thin strokes largely intact. But with high compression/low retention (34%), we observe a higher background grain and occasional breaks in tight curves, with loop digits (0/6/8) and multi-segment (5) the first to degrade. Nevertheless, class identity remains visible in most samples, with the strong speedup at this compression. Overall, CSDM achieves substantial wall-clock savings while preserving

digit identity over a wide range of compression; artifacts concentrate in thin/curved strokes at aggressive compression.

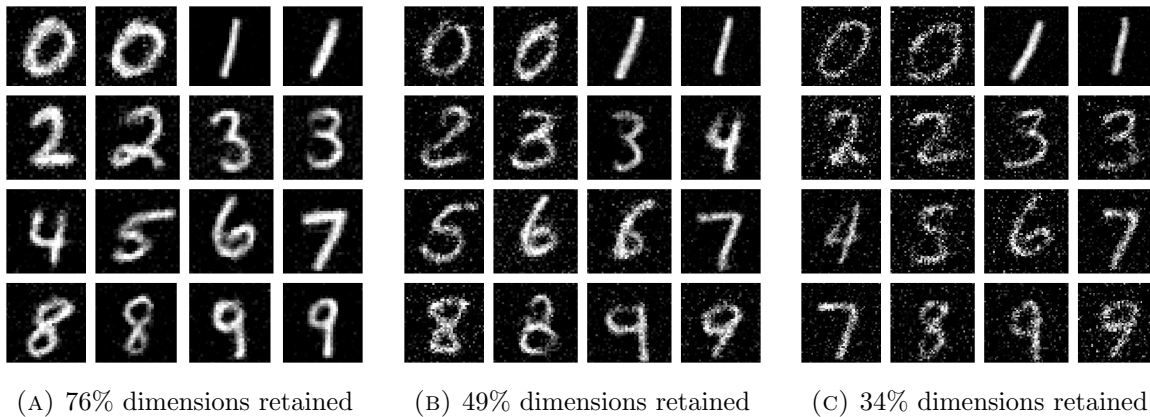


FIGURE 1. MNIST generations at three compression levels.

**4.2. Results on OCTMNIST.** OCTMNIST contains retinal OCT B-scans from the MedMNIST collection [81]. Unlike handwritten digits, medical images are generally less sparse. However, OCT exhibits banded anatomy: most diagnostic content concentrates in a narrow horizontal band (retinal layers) near the upper or middle part of the frame; while large regions, especially the lower half, are near-zero background (see Figure 2 for illustration). This induces substantial spatial sparsity, which is around 65–70% near-zero pixels at native resolution.

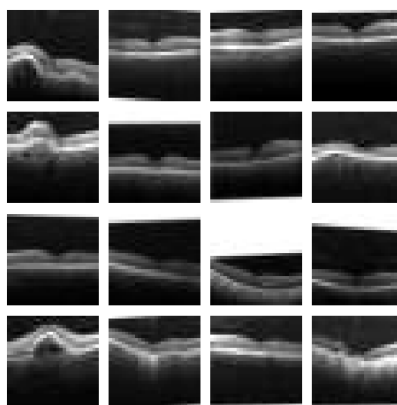


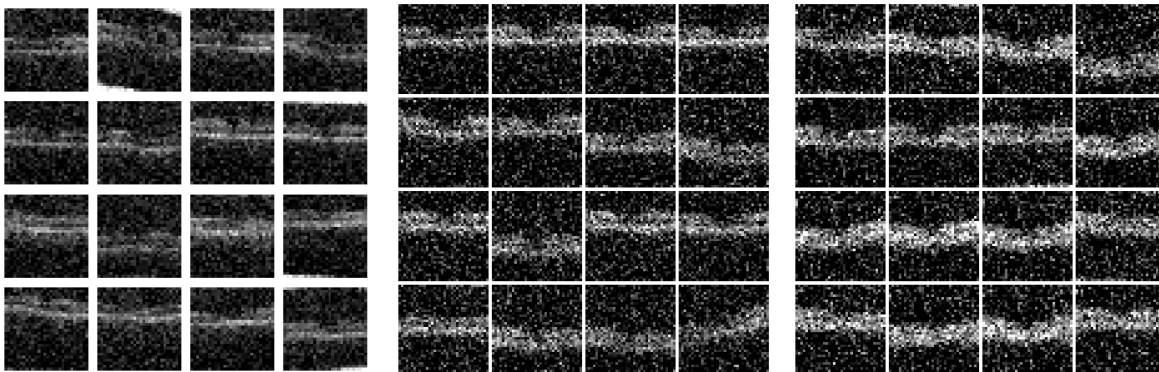
FIGURE 2. Original OCTMNIST samples

We follow the same setup as in MNIST. Table 3 reports per-image wall-clock for diffusion inference in  $\mathbb{R}^m$ , FISTA recovery in  $\mathbb{R}^d$ , along with the speedup. The result is similar to MNIST: as the dimension  $d$  increases, the diffusion inference time in the latent space stays roughly constant with the recovery adding a small overhead, which yields larger net time savings.

Compression	Original Dim.	Original Dim. Inference Time	Low Dim. Inference Time	Recovery Time	Speedup
76%	1024 → 784	1.6465s / pic	1.2606s / pic	0.1519s / pic	<b>4.99%</b>
49%	1600 → 784	1.9243s / pic	0.9429s / pic	0.1541s / pic	<b>42.99%</b>
34%	2034 → 784	2.8735s / pic	1.1076s / pic	0.1556s / pic	<b>56.04%</b>

TABLE 3. Comparison of generation time on OCTMNIST

Figure 3 shows CSDM generations at different compression levels. With low compression/high retention (76%), the retinal band is continuous and well localized; intra-band texture appears with mild grain, and the background remains largely quiescent. Layer transitions are visible, with only light speckle around boundaries. With high compression/low retention (34%), the band stays recognizable and contiguous, yet shows higher intra-band speckle and occasional softening at sharp transitions; background grain is more pronounced. Overall, CSDM preserves the banded retinal anatomy, while delivering substantial wall-clock savings. Artifacts concentrate as mild speckle and slight softening within the band at aggressive compression, but the decision-relevant structure (e.g., band continuity and localization) remains clear across settings.



(A) 77% dimensions retained

(B) 49% dimensions retained

(C) 34% dimensions retained

FIGURE 3. OCTMNIST generations at three compression levels.

**4.3. Results on ERA5 Reanalysis.** ERA5 Reanalysis dataset is provided by ECMWF on the large-scale precipitation fraction (LSPF) field (see Figure 4 for illustration). In contrast with the previous two subsections, each snapshot is resized to a fixed ambient resolution of  $80 \times 80$ , and then compressed to the retention levels 64% ( $64 \times 64$ ), 49% ( $56 \times 56$ ), and 36% ( $48 \times 48$ ).

Table 4 reports the per-sample wall-clock for diffusion inference in  $\mathbb{R}^m$ , FISTA recovery in  $\mathbb{R}^d$ , along with the speedup. As the level of compression increases, the diffusion inference time in the latent space shortens significantly with the recovery remaining lightweight; the net speedup increases steadily from 4.22% to 59.31%.

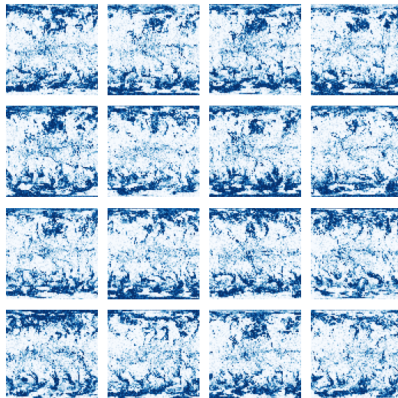


FIGURE 4. Original LSPF samples in Year 2023

Compression	Original Dim.	Original Dim. Inference Time	Low Dim. Inference Time	Recovery Time	Speedup
64%	6400 $\rightarrow$ 4096	13.7545s / pic	8.8029s / pic	4.3712s / pic	<b>4.22%</b>
49%	6400 $\rightarrow$ 3136	12.8296s / pic	6.2865s / pic	1.7669s / pic	<b>37.23%</b>
36%	6400 $\rightarrow$ 2304	12.2049s / pic	4.3938s / pic	0.5721s / pic	<b>59.31%</b>

TABLE 4. Comparison of generation time on LSPF

Figure 5 illustrates CSDM generations at different compression levels. With low compression/high retention (64%), the generations are nearly indistinguishable from the full-resolution fields. Fine-scale precipitation patterns are well preserved, with only minor smoothing in localized regions. With high compression/low retention (36%), large-scale structures are still visible, but finer details are partially lost, and small patches may merge or vanish. Overall, CSDM achieves significant wall-clock savings, while retaining essential spatial patterns on a complex and low-sparsity climate dataset. As the level of compression increases, artifacts manifest primarily in the loss of local variability, but the large-scale precipitation dynamics remain intact for downstream geophysical and risk analysis.

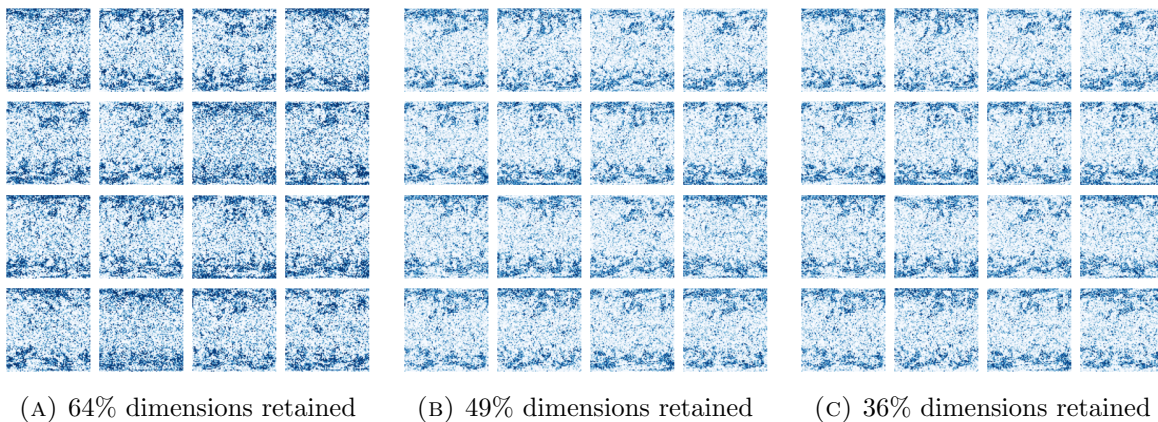


FIGURE 5. LSPF generations at three compression levels.

## 5. NUMERICAL EXPERIMENTS ON TIME SERIES DATA

In this section, we further explore the idea of integrating diffusion models with dimension reduction techniques in the context of financial time series. Previous works [1, 19] exploited diffusion models for portfolio optimization, while our focus is on stress testing. Instead of applying random projections (and compressed sensing), we use principal component analysis (PCA) to find the most significant variance directions of macroeconomic factors. We then train a diffusion model in the principle component (PC) space to generate synthetic PC data. These generated PC data can be viewed as “informative” factors, which can be subsequently used for portfolio backtesting and stress testing via regression analysis.

Here we train a diffusion model in a low-dimensional macro-factor space: the first 6 PCs computed from 126 FRED-MD factors [54], corresponding to over 90% of cumulative explained variance. We then generate synthetic PC paths, and map them to the equity space (AAPL, AMZN, COST, CVX, GOOGL, JPM, KO, MCD, NVDA, UNH) for portfolio management (Section 5.1) and stress testing (Section 5.2).

*Value at Risk (VaR)*: For a portfolio return  $R$ , the  $\alpha$ -quantile  $Q_\alpha(R)$  induces the (left-tail) VaR as

$$\text{VaR}_\alpha = -Q_\alpha(R).$$

The tables below report the quantiles of returns, with the 1%, 5%, 10% and 25% rows corresponding to  $\text{VaR}_{99\%}$ ,  $\text{VaR}_{95\%}$ ,  $\text{VaR}_{90\%}$  and  $\text{VaR}_{75\%}$  (after the sign change).

**5.1. Unconditional Portfolio Management.** We evaluate 6-month cumulative log-returns under three portfolio constructions: (i) Equal-Weight portfolio, (ii) Markowitz global minimum variance portfolio (GMVP), and (iii) Risk-Parity portfolio. If the low-dimensional PCs retain the key risk directions, then the generated data are expected to reproduce distributional properties (e.g., center, dispersion and tails).

(i) *Equal-Weight Portfolio*: Figure 6 shows the histograms of real and generated 6-month cumulative log-returns, and Table 5 provides the summary statistics.

Statistics	Real 6M	Generated 6M
Mean	9.43%	6.78%
Median	10.38%	7.62%
Std Dev	8.83%	9.13%
1% Quantile	-12.65%	-16.35%
5% Quantile	-6.64%	-10.05%
10% Quantile	-2.67%	-5.25%
25% Quantile	4.17%	1.95%

TABLE 5. Equal-weight portfolio: real vs. generated 6M log-return statistics.

The generated portfolio distribution aligns with the real one in location and scale, while showing a heavier left tail. The VaR errors are the largest for the equal-weight portfolio (e.g., the 5% quantile differs by  $\approx 3.41\text{pp}$ ), indicating more mass in the synthetic left tail with no risk-adjusted weights.

(ii) *Markowitz GMVP*: Table 6 provides the GMVP weights (with short-selling not allowed), and Figure 7 shows the histograms of real and generated log-returns. The summary statistics (Table 7) and the efficient frontiers (Figure 9) show that the real and generated portfolios have close mean and volatilities, but moderate tail differences. Also note that GMVP tails are much closer than those in the equal-weight case (e.g.,  $|\Delta Q_{1\%}| \approx 0.62\text{pp}$  and  $|\Delta Q_{5\%}| \approx 1.03\text{pp}$ ), suggesting that the PC diffusion generations preserve the covariance structure relevant to volatility minimization.

Source	AAPL	AMZN	COST	CVX	GOOGL
Real (%)	0.00	4.74	17.83	1.61	9.47
Generated (%)	0.00	1.35	28.85	2.47	6.05
Source	JPM	KO	MCD	NVDA	UNH
Real (%)	1.45	27.99	25.34	0.00	11.56
Generated (%)	0.00	39.40	13.39	0.00	10.96

TABLE 6. GMVP portfolio weights comparison (real vs. generated).

Statistics	Real GMVP	Predicted GMVP
Mean	7.26%	7.28%
Median	7.63%	7.01%
Std Dev	6.19%	6.42%
1% Quantile	-8.52%	-7.90%
5% Quantile	-2.78%	-3.81%
10% Quantile	-0.26%	-0.73%
25% Quantile	3.65%	3.52%

TABLE 7. GMVP: real vs. generated 6M log-return statistics.

(iii) *Risky-Parity Portfolio*: Table 8 reports the risk-parity weights, which are similar in both settings. Figure 8 provides the histograms of real and generated log-returns. The summary statistics (Table 9) shows that mean and volatilities match, and the left-tail quantiles differ by only 0.01–0.04pp, indicating that tail risk is effectively captured when portfolios are constructed from risk-balanced exposures.

Source	AAPL	AMZN	COST	CVX	GOOGL
Real (%)	7.90	8.37	11.56	9.05	9.23
Generated (%)	7.31	8.62	12.29	9.04	9.43
Source	JPM	KO	MCD	NVDA	UNH
Real (%)	8.23	14.67	14.27	5.42	11.30
Generated (%)	8.50	14.71	13.50	5.14	11.46

TABLE 8. Risk-Parity portfolio weights comparison (real vs. generated).

Statistics	Real RP	Predicted RP
Mean	8.55%	8.54%
Median	8.85%	8.71%
Std Dev	7.43%	7.41%
1% Quantile	-11.33%	-11.32%
5% Quantile	-3.47%	-3.51%
10% Quantile	-1.48%	-1.46%
25% Quantile	4.00%	4.17%

TABLE 9. Risk-Parity: real vs. generated 6M log-return statistics.

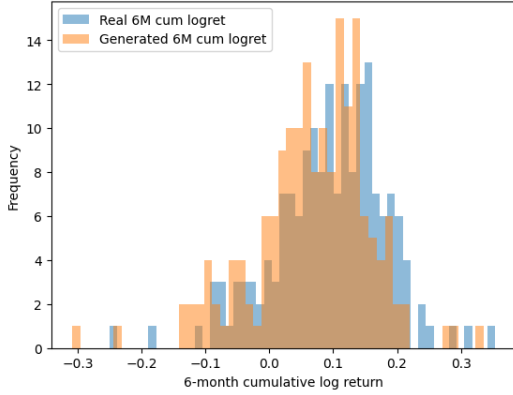


FIGURE 6. Equal-weight portfolio comparison.

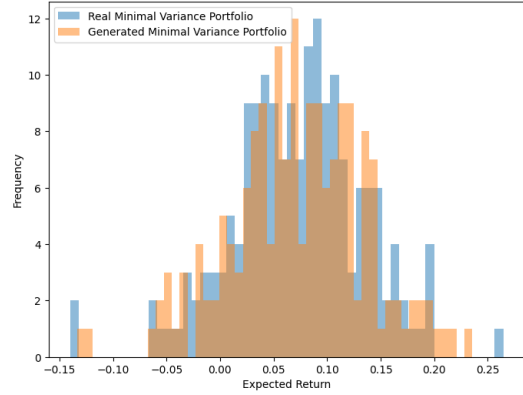


FIGURE 7. GMVP comparison.

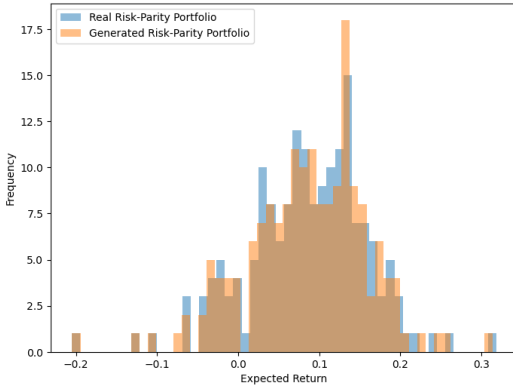


FIGURE 8. Risk-parity comparison.

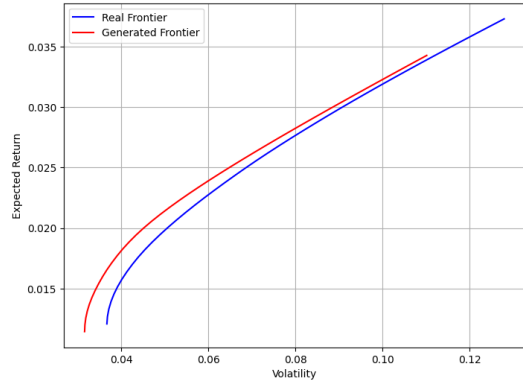


FIGURE 9. Efficient frontiers comparison.

Overall, training a diffusion model in a low-dimensional macro-PC space has proven reliable in reproducing the real data distribution for backtesting across equal-weight, GMVP, and risk-parity portfolios, and crucially, the left-tail quantiles are close to their empirical counterparts.

Weight patterns are consistent for GMVP and risk-parity, indicating that the low-dimensional PCs retain the covariance structure that drives risk-aware portfolio construction.

**5.2. Standard scenario analysis (SSA).** *Standard scenario analysis* (SSA) for financial portfolios is designed to estimate a portfolio’s return when some subsets of risk factors are subjected to stress [32]. Here we follow the presentation of [2].

Under the standard multi-factor model for stock returns, if  $X_t \in \mathbb{R}^d$  is the  $d$ -dimensional vector of common factors, we define  $\mathcal{S}$  to be the set containing the indices of the factors in a scenario (i.e., the factors that we intend to stress), and hence  $\mathcal{S}^c$  is the index set of those factors that we leave un-stressed. SSA stresses the components of  $X_{S,t}$  according to a given scenario (e.g., +20 on the S&P index, −10 on the CPI index, and +0.1 on the US Dollar/Euro exchange rate), and keeps the components in  $X_{S^c,t}$  unchanged (i.e., equal to their current value). The new portfolio P&L, or overall return  $V_t$  is then computed with  $Y_t$  determined by the scenario and the multi-factor model. To be more precise,

- (1) Let  $\Delta X_{S,t+1} = X_{S,t+1} - X_{S,t}$  denote the  $t + 1$  scenario stress vector  $\in \mathbb{R}^{|\mathcal{S}|}$ .
- (2) Compute the SSA factor change vector:

$$\Delta X_{i,t+1}^{SSA} = \begin{cases} \Delta X_{S,t+1}, & \text{for } i \in \mathcal{S}, \\ 0, & \text{for } i \in \mathcal{S}^c. \end{cases}$$

- (3) Obtain the predicted factor vector under SSA:  $X_{t+1}^{SSA} = X_t + \Delta X_{t+1}^{SSA}$ .
- (4) From the fitted neural net  $f_{NN}$ , predict the post-stress asset returns:  $Y_{t+1}^{SSA-\text{stress}} = f_{NN}(X_{t+1}^{SSA})$ .

We summarize the SSA procedure in the following algorithm, which we will later feed into a historical rolling window backtest. Let  $s$  be the size of the rolling window. Note that the fitted matrix of factor loadings,  $f_{NN}$  is treated as an input in this algorithmic format. Denote by  $x_{t-s:t} \in \mathbb{R}^{s \times p}$  the matrix of common factors from time  $t - s$  up to  $t$ , and by  $y_{t-s:t} \in \mathbb{R}^{s \times n}$  the matrix of asset returns from time  $t - s$  up to  $t$ . We take  $x_{\text{actual},S,t+1}$  to be the realized historical scenario.

**Input:**  $x_{t-s:t}$  (common factors in rolling window),  $x_{t+1}$  (future factors),  $f_{NN}$  (neural net fitted on the whole time series)

**Output:**  $\hat{V}_{t+1,SSA}$  (portfolio return under SSA)

- (1) Set  $x_{S,t+1} \leftarrow x_{\text{actual},S,t+1}$  and  $x_{S^c,t+1} \leftarrow x_{S^c,t}$  to form  $x_{t+1}^{SSA}$ .
- (2) Compute  $y_{t+1,SSA} \leftarrow f_{NN}(x_{t+1}^{SSA})$ .
- (3) Compute portfolio weights  $w \leftarrow 1/N$  (or Markowitz weights, or Risk-Parity).
- (4) Compute portfolio return  $\hat{V}_{t+1,SSA} \leftarrow w^\top y_{t+1,SSA}$ .

In our experiments, the goal is to evaluate the performance of the generated data against real data in the context of financial stress testing. For the real data, we train a neural network model  $f_{NN}^{\text{macro}}$ , where the input consists of 126 macroeconomic factors. In this setting, the variable  $x^{SSA}$  in the aforementioned algorithm corresponds directly to these macro factors. The generated data are constructed from the first six principal components (PCs). To process these synthetic features, we employ a different neural net  $f_{NN}^{\text{PC}}$ , which takes as input the time

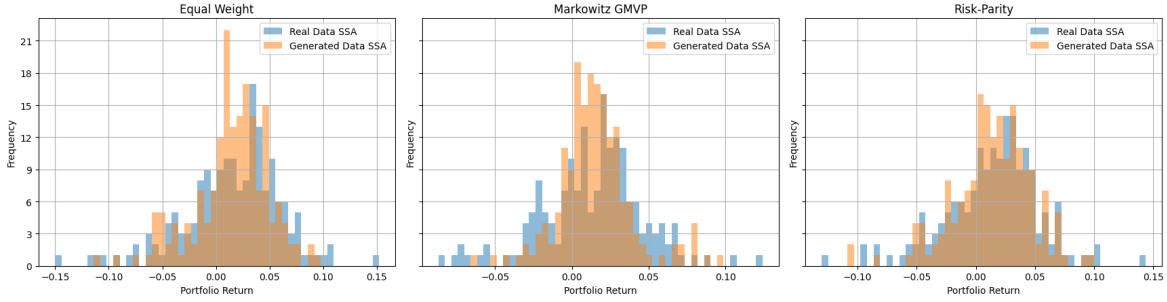


FIGURE 10. Real vs. Generated SSA (Scenario 1: RPI &amp; SRVPRD)

series of six PCs, and outputs the corresponding stock prices. In this case,  $x^{SSA}$  are the values of the principal components instead of the original macroeconomic factors.

We conduct SSA by stressing selected macro factors while holding all others fixed, and then computing portfolio returns under three strategies: Equal Weight, Markowitz GMVP, and Risk-Parity. We compare *Real Data SSA* (macro factors fed to a neural net trained on all 126 factors) with *Generated Data SSA* (diffusion inference in the PC space). Three scenarios are considered: (1) RPI + SRVPRD; (2) S&P 500 + ACOGNO; (3) all four (RPI, SRVPRD, S&P 500, ACOGNO). Figures 10–12 illustrate the empirical return distributions under the two data sources. Across all strategies and scenarios, the generated distributions exhibit strong alignment with the real data benchmarks in terms of central tendency, dispersion, and tail behavior. This is further confirmed by detailed summary statistics in Tables 10–12. Notably, under the GMVP strategy, the generated data reproduce the real mean return within a margin of less than 0.2%, while the extreme quantiles (1%, 5%) also display high fidelity, suggesting accurate modeling of downside risks. Similar consistency is observed for the risk-parity strategy, where the generated returns track both the scale and distributional shape of real data.

Method	Source	mean	median	std	1%	5%	10%	25%
Equal Weight	Real Data SSA	0.015499	0.020229	0.045045	-0.111204	-0.061352	-0.041970	-0.008881
Equal Weight	Generated Data SSA	0.014896	0.018448	0.034625	-0.078333	-0.053042	-0.037523	0.001501
Markowitz GMVP	Real Data SSA	0.013717	0.018585	0.033267	-0.073650	-0.038906	-0.026783	-0.004122
Markowitz GMVP	Generated Data SSA	0.015070	0.013561	0.023838	-0.042804	-0.021070	-0.008217	0.003035
Risk-Parity	Real Data SSA	0.014376	0.018989	0.040037	-0.096461	-0.053468	-0.037086	-0.007106
Risk-Parity	Generated Data SSA	0.013583	0.015629	0.033125	-0.089767	-0.047309	-0.025966	-0.003006

TABLE 10. Summary statistics for Scenario 1 (RPI + SRVPRD).

## 6. CONCLUSION

This paper develops dimension reduction techniques to accelerate diffusion model inference for data generation. The idea is to incorporate compressed sensing into diffusion sampling, which facilitates the efficiency of both model training and inference. Under suitable sparsity assumptions on data, the proposed CSDM algorithm is proved to enjoy faster convergence, and an optimal value for the latent space dimension is derived as a byproduct. We also

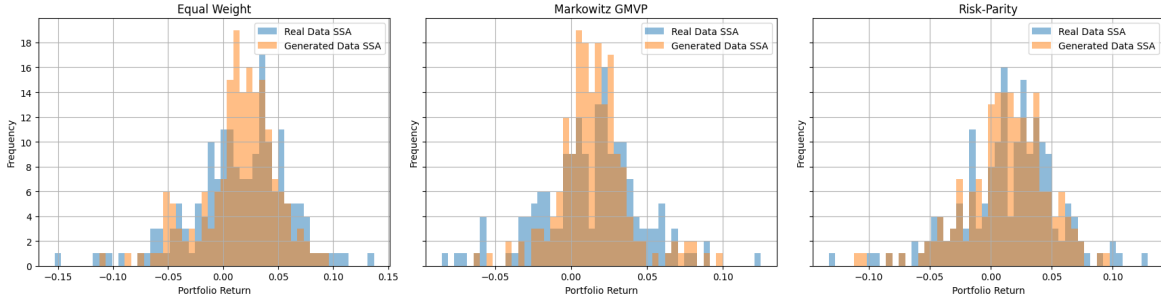


FIGURE 11. Real vs. Generated SSA (Scenario 2: S&amp;P 500 + ACOGNO).

Method	Source	mean	median	std	1%	5%	10%	25%
Equal Weight	Real Data SSA	0.015336	0.020786	0.044551	-0.110215	-0.061371	-0.041356	-0.008964
Equal Weight	Generated Data SSA	0.014808	0.018311	0.033909	-0.078462	-0.049675	-0.040138	0.001706
Markowitz GMVP	Real Data SSA	0.013588	0.018453	0.032662	-0.073197	-0.039339	-0.026637	-0.004582
Markowitz GMVP	Generated Data SSA	0.015042	0.014135	0.023652	-0.042127	-0.021630	-0.008526	0.003317
Risk-Parity	Real Data SSA	0.014182	0.018976	0.039558	-0.095410	-0.052677	-0.036798	-0.007377
Risk-Parity	Generated Data SSA	0.013485	0.015349	0.032551	-0.086335	-0.040740	-0.026172	-0.000841

TABLE 11. Summary statistics for Scenario 2 (S&amp;P 500 + ACOGNO).

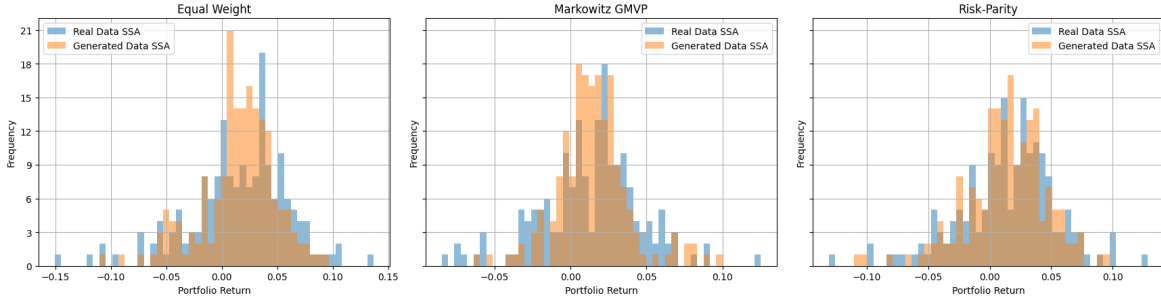


FIGURE 12. Real vs. Generated SSA (Scenario 3: RPI, SRVPRD, S&amp;P 500, ACOGNO).

Method	Source	mean	median	std	1%	5%	10%	25%
Equal Weight	Real Data SSA	0.015177	0.018720	0.044467	-0.110243	-0.061746	-0.041088	-0.009005
Equal Weight	Generated Data SSA	0.014738	0.018579	0.034219	-0.079646	-0.051498	-0.040804	0.001805
Markowitz GMVP	Real Data SSA	0.013350	0.017684	0.032525	-0.070224	-0.037711	-0.026908	-0.004720
Markowitz GMVP	Generated Data SSA	0.014791	0.014446	0.023785	-0.043476	-0.021829	-0.009040	0.003186
Risk-Parity	Real Data SSA	0.014034	0.017923	0.039447	-0.095408	-0.052755	-0.037053	-0.007807
Risk-Parity	Generated Data SSA	0.013469	0.014923	0.033141	-0.087174	-0.042830	-0.027617	-0.001268

TABLE 12. Summary statistics for Scenario 3 (all four factors).

corroborate our theory with numerical experiments on various image data, and financial time series for stress testing applications.

There are several directions to extend this work. First, an important problem is to derive sharper convergence rates of FISTA with explicit dimension dependence. This will allow us

to obtain better complexity of the proposed CSDM algorithm. Second, it is interesting to integrate the proposed CSDM algorithm into conditional generation or guidance [24, 35, 39, 71], and diffusion model alignment [6, 26, 83]. Finally, it is desirable to build a theory of PCA + diffusion models framework proposed in Section 5.

**Acknowledgment:** Wenpin Tang is supported by NSF grant DMS-2206038, the Columbia Innovation Hub grant, and the Tang Family Assistant Professorship. David D. Yao is part of a Columbia-CityU/HK collaborative project that is supported by InnoHK Initiative, The Government of the HKSAR and the AIFT Lab.

## REFERENCES

- [1] A. Aghapour, E. Bayraktar, and F. Yuan. Solving dynamic portfolio selection problems via score-based diffusion models. 2025. arXiv:2507.09916.
- [2] G. Baker, A. Capponi, and J. A. Sidaoui. Data-driven dynamic factor modeling via manifold learning. 2025. arXiv:2506.19945.
- [3] A. Beck and M. Teboulle. A fast iterative shrinkage-thresholding algorithm for linear inverse problems. *SIAM J. Imaging Sci.*, 2(1):183–202, 2009.
- [4] A. Beck and M. Teboulle. A fast iterative shrinkage-thresholding algorithm with application to wavelet-based image deblurring. In *ICASSP*, pages 693–696, 2009.
- [5] J. Benton, V. De Bortoli, A. Doucet, and G. Deligiannidis. Nearly  $d$ -linear convergence bounds for diffusion models via stochastic localization. In *ICLR*, 2024.
- [6] K. Black, M. Janner, Y. Du, I. Kostrikov, and S. Levine. Training diffusion models with reinforcement learning. In *ICLR*, 2024.
- [7] J. Bolte, T. P. Nguyen, J. Peypouquet, and B. W. Suter. From error bounds to the complexity of first-order descent methods for convex functions. *Math. Program.*, 165(2):471–507, 2017.
- [8] A. Bora, A. Jalal, E. Price, and A. G. Dimakis. Compressed sensing using generative models. In *ICML*, pages 537–546, 2017.
- [9] E. J. Candès. Compressive sampling. In *International Congress of Mathematicians. Vol. III*, pages 1433–1452. Eur. Math. Soc., Zürich, 2006.
- [10] E. J. Candès, J. Romberg, and T. Tao. Robust uncertainty principles: exact signal reconstruction from highly incomplete frequency information. *IEEE Trans. Inform. Theory*, 52(2):489–509, 2006.
- [11] E. J. Candès, J. K. Romberg, and T. Tao. Stable signal recovery from incomplete and inaccurate measurements. *Comm. Pure Appl. Math.*, 59(8):1207–1223, 2006.
- [12] E. J. Candes and T. Tao. Decoding by linear programming. *IEEE Trans. Inform. Theory*, 51(12):4203–4215, 2005.
- [13] E. J. Candes and T. Tao. Near-optimal signal recovery from random projections: universal encoding strategies? *IEEE Trans. Inform. Theory*, 52(12):5406–5425, 2006.
- [14] E. J. Candès, M. B. Wakin, and S. P. Boyd. Enhancing sparsity by reweighted  $l_1$  minimization. *J. Fourier Anal. Appl.*, 14(5-6):877–905, 2008.
- [15] A. Chambolle, R. A. DeVore, N.-y. Lee, and B. J. Lucier. Nonlinear wavelet image processing: variational problems, compression, and noise removal through wavelet shrinkage. *IEEE Trans. Image Process.*, 7(3):319–335, 1998.
- [16] R. Chartrand and W. Yin. Iteratively reweighted algorithms for compressive sensing. In *ICASSP*, pages 3869–3872, 2008.
- [17] M. Chen, K. Huang, T. Zhao, and M. Wang. Score approximation, estimation and distribution recovery of diffusion models on low-dimensional data. In *ICML*, pages 4672–4712, 2023.
- [18] M. Chen, K. Huang, T. Zhao, and M. Wang. Score approximation, estimation and distribution recovery of diffusion models on low-dimensional data. In *ICML*, volume 40, pages 4672–4712, 2023.
- [19] M. Chen, R. Xu, Y. Xu, and R. Zhang. Diffusion factor models: Generating high-dimensional returns with factor structure. 2025. arXiv:2504.06566.
- [20] S. Chen, S. Chewi, H. Lee, Y. Li, J. Lu, and A. Salim. The probability flow ODE is provably fast. In *Neurips*, volume 36, pages 68552–68575, 2023.

- [21] S. Chen, S. Chewi, J. Li, Y. Li, A. Salim, and A. R. Zhang. Sampling is as easy as learning the score: theory for diffusion models with minimal data assumptions. In *ICLR*, 2023.
- [22] S. S. Chen, D. L. Donoho, and M. A. Saunders. Atomic decomposition by basis pursuit. *SIAM J. Sci. Comput.*, 20(1):33–61, 1998.
- [23] I. Daubechies, M. Defrise, and C. De Mol. An iterative thresholding algorithm for linear inverse problems with a sparsity constraint. *Comm. Pure Appl. Math.*, 57(11):1413–1457, 2004.
- [24] P. Dhariwal and A. Nichol. Diffusion models beat GANs on image synthesis. In *Neurips*, volume 34, pages 8780–8794, 2021.
- [25] D. L. Donoho. Compressed sensing. *IEEE Trans. Inform. Theory*, 52(4):1289–1306, 2006.
- [26] Y. Fan, O. Watkins, Y. Du, H. Liu, M. Ryu, C. Boutilier, P. Abbeel, M. Ghavamzadeh, K. Lee, and K. Lee. DPOK: Reinforcement learning for fine-tuning text-to-image diffusion models. In *Neurips*, volume 36, pages 79858–79885, 2023.
- [27] X. Gao, H. M. Nguyen, and L. Zhu. Wasserstein convergence guarantees for a general class of score-based generative models. *J. Mach. Learn. Res.*, 26(43):1–54, 2025.
- [28] X. Gao and L. Zhu. Convergence analysis for general probability flow odes of diffusion models in wasserstein distances. In *AISTATS*, pages 1009–1017, 2025.
- [29] Google. State-of-the-art video and image generation with Veo 2 and Imagen 3. 2024. Available at <https://blog.google/technology/google-labs/video-image-generation-update-december-2024/>.
- [30] I. F. Gorodnitsky and B. D. Rao. Sparse signal reconstruction from limited data using focuss: A re-weighted minimum norm algorithm. *IEEE Trans. Signal Process.*, 45(3):600–616, 2002.
- [31] Y. Han, M. Razaviyayn, and R. Xu. Neural network-based score estimation in diffusion models: Optimization and generalization. In *ICLR*, 2024.
- [32] M. B. Haugh and O. Ruiz Lacedelli. Scenario analysis for derivative portfolios via dynamic factor models. *Quant. Finance*, 20(4):547–571, 2020.
- [33] U. G. Haussmann and E. Pardoux. Time reversal of diffusions. *Ann. Probab.*, 14(4):1188–1205, 1986.
- [34] J. Ho, A. Jain, and P. Abbeel. Denoising diffusion probabilistic models. In *Neurips*, volume 33, pages 6840–6851, 2020.
- [35] J. Ho and T. Salimans. Classifier-free diffusion guidance. In *NeurIPS Workshop on Deep Generative Models and Downstream Applications*, 2021.
- [36] Z. Huang, Y. Wei, and Y. Chen. Denoising diffusion probabilistic models are optimally adaptive to unknown low dimensionality. 2024. arXiv:2410.18784.
- [37] P. R. Johnstone and P. Moulin. A lyapunov analysis of fista with local linear convergence for sparse optimization. 2015. arXiv:1502.02281.
- [38] T. Karras, M. Aittala, T. Aila, and S. Laine. Elucidating the design space of diffusion-based generative models. In *Neurips*, volume 35, pages 26565–26577, 2022.
- [39] T. Karras, M. Aittala, T. Kynkäänniemi, J. Lehtinen, T. Aila, and S. Laine. Guiding a diffusion model with a bad version of itself. In *Neurips*, volume 37, pages 52996–53021, 2024.
- [40] S. Khanna, S. Kharbanda, S. Li, H. Varma, E. Wang, S. Birnbaum, Z. Luo, Y. Miraoui, A. Palrecha, and S. Ermon. Mercury: Ultra-fast language models based on diffusion. 2025. arXiv:2506.17298.
- [41] D. Kingma, T. Salimans, B. Poole, and J. Ho. Variational diffusion models. In *Neurips*, volume 34, pages 21696–21707, 2021.
- [42] Z. Kong, W. Ping, J. Huang, K. Zhao, and B. Catanzaro. Diffwave: A versatile diffusion model for audio synthesis. In *ICLR*, 2021.
- [43] C. Kümmerle, C. Mayrink Verdun, and D. Stöger. Iteratively reweighted least squares for basis pursuit with global linear convergence rate. In *Neurips*, volume 34, pages 2873–2886, 2021.
- [44] Y. LeCun, L. Bottou, Y. Bengio, and P. Haffner. Gradient-based learning applied to document recognition. *Proc. of the IEEE*, 86(11):2278–2324, 1998.
- [45] H. Lee, J. Lu, and Y. Tan. Convergence for score-based generative modeling with polynomial complexity. In *Neurips*, volume 35, pages 22870–22882, 2022.
- [46] G. Li, Y. Huang, T. Efimov, Y. Wei, Y. Chi, and Y. Chen. Accelerating convergence of score-based diffusion models, provably. In *ICML*, pages 27942–27954, 2024.
- [47] G. Li, Y. Wei, Y. Chen, and Y. Chi. Towards faster non-asymptotic convergence for diffusion-based generative models. In *ICLR*, 2024.

- [48] G. Li and Y. Yan. Adapting to unknown low-dimensional structures in score-based diffusion models. In *Neurips*, volume 37, pages 126297–126331, 2024.
- [49] G. Li and Y. Yan.  $O(d/t)$  convergence theory for diffusion probabilistic models under minimal assumptions. In *ICLR*, 2025.
- [50] Y. Lipman, R. T. Chen, H. Ben-Hamu, M. Nickel, and M. Le. Flow matching for generative modeling. In *ICLR*, 2023.
- [51] X. Liu, C. Gong, and Q. Liu. Flow straight and fast: Learning to generate and transfer data with rectified flow. In *ICLR*, 2022.
- [52] C. Lu, Y. Zhou, F. Bao, J. Chen, C. Li, and J. Zhu. DPM-Solver: A fast ODE solver for diffusion probabilistic model sampling in around 10 steps. In *NeurIPS*, pages 5775–5787, 2022.
- [53] N. Ma, S. Tong, H. Jia, H. Hu, Y.-C. Su, M. Zhang, X. Yang, Y. Li, T. Jaakkola, and X. Jia. Inference-time scaling for diffusion models beyond scaling denoising steps. 2025. arXiv:2501.09732.
- [54] M. W. McCracken and S. Ng. Fred-md: A monthly database for macroeconomic research. *J. Bus. Econ. Stat.*, 34(4):574–589, 2016.
- [55] B. K. Natarajan. Sparse approximate solutions to linear systems. *SIAM J. Comput.*, 24(2):227–234, 1995.
- [56] S. Nie, F. Zhu, Z. You, X. Zhang, J. Ou, J. Hu, J. Zhou, Y. Lin, J.-R. Wen, and C. Li. Large language diffusion models. 2025. arXiv:2502.09992.
- [57] OpenAI. Sora: Creating video from text. 2024. Available at <https://openai.com/sora>.
- [58] P. Pope, C. Zhu, A. Abdelkader, M. Goldblum, and T. Goldstein. The intrinsic dimension of images and its impact on learning. In *ICLR*, 2021.
- [59] P. Potapchik, I. Azangulov, and G. Deligiannidis. Linear convergence of diffusion models under the manifold hypothesis. 2024. arXiv:2410.09046.
- [60] A. Ramesh, P. Dhariwal, A. Nichol, C. Chu, and M. Chen. Hierarchical text-conditional image generation with clip latents. 2022. arXiv:2204.06125.
- [61] R. Rombach, A. Blattmann, D. Lorenz, P. Esser, and B. Ommer. High-resolution image synthesis with latent diffusion models. In *CVPR*, pages 10684–10695, 2022.
- [62] M. Rudelson and R. Vershynin. Non-asymptotic theory of random matrices: extreme singular values. In *Proceedings of the International Congress of Mathematicians. Volume III*, pages 1576–1602. Hindustan Book Agency, New Delhi, 2010.
- [63] T. Salimans and J. Ho. Progressive distillation for fast sampling of diffusion models. In *ICLR*, 2022.
- [64] U. Singer, A. Polyak, T. Hayes, X. Yin, J. An, S. Zhang, Q. Hu, H. Yang, O. Ashual, and O. Gafni. Make-a-video: Text-to-video generation without text-video data. In *ICLR*, 2023.
- [65] J. Song, C. Meng, and S. Ermon. Denoising diffusion implicit models. In *ICLR*, 2021.
- [66] Y. Song and P. Dhariwal. Improved techniques for training consistency models. In *ICLR*, 2024.
- [67] Y. Song, P. Dhariwal, M. Chen, and I. Sutskever. Consistency models. In *ICML*, pages 32211–32252, 2023.
- [68] Y. Song and S. Ermon. Generative modeling by estimating gradients of the data distribution. In *Neurips*, volume 32, 2019.
- [69] Y. Song, J. Sohl-Dickstein, D. P. Kingma, A. Kumar, S. Ermon, and B. Poole. Score-based generative modeling through stochastic differential equations. In *ICLR*, 2021.
- [70] D. W. Stroock and S. R. S. Varadhan. *Multidimensional diffusion processes*, volume 233 of *Grundlehren der Mathematischen Wissenschaften*. Springer-Verlag, 1979.
- [71] W. Tang and R. Xu. A stochastic analysis approach to conditional diffusion guidance. 2025. Working paper. Available at <https://www.columbia.edu/~wt2319/CDG.pdf>.
- [72] W. Tang and H. Zhao. Contractive diffusion probabilistic models. 2024. arXiv:2401.13115.
- [73] W. Tang and H. Zhao. Score-based diffusion models via stochastic differential equations. *Statist. Surv.*, 19:28–64, 2025.
- [74] S. Tao, D. Boley, and S. Zhang. Local linear convergence of ISTA and FISTA on the LASSO problem. *SIAM J. Optim.*, 26(1):313–336, 2016.
- [75] E. van den Berg and M. P. Friedlander. Probing the Pareto frontier for basis pursuit solutions. *SIAM J. Sci. Comput.*, 31(2):890–912, 2008.
- [76] R. Vershynin. On the role of sparsity in compressed sensing and random matrix theory. In *CAMSAP*, pages 189–192, 2009.

- [77] P. Vincent. A connection between score matching and denoising autoencoders. *Neural Comput.*, 23(7):1661–1674, 2011.
- [78] Y. Wang, Y. He, and M. Tao. Evaluating the design space of diffusion-based generative models. In *Neurips*, volume 37, pages 19307–19352, 2024.
- [79] G. I. Winata, H. Zhao, A. Das, W. Tang, D. D. Yao, S.-X. Zhang, and S. Sahu. Preference tuning with human feedback on language, speech, and vision tasks: A survey. *J. Artif. Intell. Res.*, 82:2595–2661, 2025.
- [80] X. Xu and Y. Chi. Provably robust score-based diffusion posterior sampling for plug-and-play image reconstruction. In *Neurips*, volume 37, pages 36148–36184, 2024.
- [81] J. Yang, R. Shi, D. Wei, Z. Liu, L. Zhao, B. Ke, H. Pfister, and B. Ni. MedMNIST v2—a large-scale lightweight benchmark for 2d and 3d biomedical image classification. *Sci. Data*, 10(1):41, 2023.
- [82] Q. Zhang and Y. Chen. Fast sampling of diffusion models with exponential integrator. In *ICLR*, 2023.
- [83] H. Zhao, H. Chen, J. Zhang, D. Yao, and W. Tang. Score as Action: Fine tuning diffusion generative models by continuous-time reinforcement learning. In *ICML*, 2025.

DEPARTMENT OF INDUSTRIAL ENGINEERING AND OPERATIONS RESEARCH, COLUMBIA UNIVERSITY.

*Email address:* `zg2525@columbia.edu`

DEPARTMENT OF STATISTICS, COLUMBIA UNIVERSITY.

*Email address:* `j16969@columbia.edu`

DEPARTMENT OF INDUSTRIAL ENGINEERING AND OPERATIONS RESEARCH, COLUMBIA UNIVERSITY.

*Email address:* `wt2319@columbia.edu`

DEPARTMENT OF INDUSTRIAL ENGINEERING AND OPERATIONS RESEARCH, COLUMBIA UNIVERSITY.

*Email address:* `ddy1@columbia.edu`